

Verification of multi-structure targeting in chronic microelectrode brain recordings from CT scans

Luciano Censori^a, Pär Halje^b, Jan Axelsson^c, Katrine Skovgård^{b,d}, Arash Ramezani^a, Evgenya Malinina^a, Per Petersson^{a,b,*}

^a Department of Integrative Medical Biology, Umeå University, Umeå, Sweden

^b The Group for Integrative Neurophysiology and Neurotechnology, Department of Experimental Medical Science, Lund University, Lund, Sweden

^c Department of Radiation Science, Umeå University, Umeå, Sweden

^d Basal Ganglia Pathophysiology Unit, Department of Experimental Medical Science, Lund University, Lund, Sweden

ARTICLE INFO

Keywords:

X-ray
Imaging
Rat
Mouse
Microelectrode
Neurophysiology

ABSTRACT

Background: Large-scale microelectrode recordings offer a unique opportunity to study neurophysiological processes at the network level with single cell resolution. However, in the small brains of many experimental animals, it is often technically challenging to verify the correct targeting of the intended structures, which inherently limits the reproducibility of acquired data.

New method: To mitigate this problem, we have developed a method to programmatically segment the trajectory of electrodes arranged in larger arrays from acquired CT-images and thereby determine the position of individual recording tips with high spatial resolution, while also allowing for coregistration with an anatomical atlas, without pre-processing of the animal samples or post-imaging histological analyses.

Results: Testing the technical limitations of the developed method, we found that the choice of scanning angle influences the achievable spatial resolution due to shadowing effects caused by the electrodes. However, under optimal acquisition conditions, individual electrode tip locations within arrays with 250 µm inter-electrode spacing were possible to reliably determine.

Comparison to existing methods: Comparison to a histological verification method suggested that, under conditions where individual wires are possible to track in slices, a 90% correspondence could be achieved in terms of the number of electrodes groups that could be reliably assigned to the same anatomical structure.

Conclusions: The herein reported semi-automated procedure to verify anatomical targeting of brain structures in the rodent brain could help increasing the quality and reproducibility of acquired neurophysiological data by reducing the risk of assigning recorded brain activity to incorrectly identified anatomical locations.

Data availability: The tools developed in this study are freely available as a software package at: <https://github.com/NRC-Lund/ct-tools>

1. Introduction

It is increasingly being recognized that several important brain functions can only be studied in awake behaving subjects; for example, the physiological processes underlying selection of behaviors, learning and memory functions, as well as a range of symptoms in animal models of neurologic/psychiatric disease and the therapeutic mechanisms of existing and novel treatment approaches. In parallel, rapid technological developments during recent years have opened up for several new ways to assess brain functions in the intact nervous system. For example, new

designs of large-scale microelectrode recordings now allow for recordings of hundreds or even thousands of neurons in parallel also in the brain of small experimental animals such as rats and mice (Dzirasa et al., 2011; Ivica et al., 2014; Steinmetz et al., 2018). For cortical electrodes, reliable targeting of the intended areas and depths can often be carried out with standardized stereotactic techniques (Campbell et al., 1991; Schwarz et al., 2014). However, brain functions are highly distributed and the coordinated action of cortical circuits crucially depends on neurophysiological processes of subcortical structures such as the thalamus and basal ganglia. Thus, to investigate circuit-level processes,

* Correspondence to: Integrativ medicinsk biologi, Johan Bures väg 12, Biologihuset, 901 87 Umeå, Sweden.

E-mail address: Per.Petersson@umu.se (P. Petersson).

<https://doi.org/10.1016/j.jneumeth.2022.109719>

Received 23 March 2022; Received in revised form 7 September 2022; Accepted 29 September 2022

Available online 3 October 2022

0165-0270/© 2022 The Authors. Published by Elsevier B.V. This is an open access article under the CC BY license (<http://creativecommons.org/licenses/by/4.0/>).

parallel targeting of cortical structures together with deeper targets is needed (Tamtè et al., 2016). Notably, however, due to inter-individual anatomical variation among experimental animals, limitations in the geometrical precision of multi-channel electrode constructions and occasional human errors during surgical procedures, some electrodes will inevitably miss their intended targets.

To improve the reliability and validity of microelectrode data collected from several small brain structures in parallel, it is necessary to be able to verify the location of the recording point of each electrode in the implanted brain. To verify appropriate electrode location, post mortem tissue analyses are typically performed using Nissl staining of brain sections (Stensola et al., 2012; Hanson et al., 2019) and when a smaller number of electrodes are used, electrolytic lesions, dye coating of electrodes etc. can help to further improve precision. For electrode designs including over 100 recording sites in complex geometries and at varying depths, however, this task becomes increasingly difficult using traditional histological techniques. To circumvent this problem, we have here made use of the gradually more widely available Computed Tomography (CT) imaging systems for small animals, to develop a semi-automatized system allowing for the identification of individual electrode tip locations in small brains. Furthermore, we evaluated its functionality for chronically implanted multi-channel electrodes consisting of 128 individual recording electrodes distributed over 10 distinct brain structures in each hemisphere in adult rats, and 32 recording electrodes distributed over 4 structures per hemisphere in an adult mouse, respectively.

2. Materials and methods

2.1. Animals used

Seven adult female Sprague-Dawley rats (250–300 g; from Janvier Labs or in-house colony in Umeå) and 1 adult female B6 (PV^{cre}) mouse (20 g; Jackson lab stock no: 017320) were used in the present study. Animals were part of ongoing studies in our two labs located at Lund/Umeå University, Sweden. Animals were kept on a 12:12 h light cycle and received food and water ad libitum. All experiments were approved in advance by the Malmö/Lund and Umeå ethical committee of animal experiments. All scans included herein were obtained *post mortem* following implantation times of approximately 2–3 months. Because only female rats were included in the study, the inter-individual variation caused by differences in weight gain during the recording period was however relatively minor.

2.2. Electrode design

Multi-wire electrodes were constructed according to previously described procedures (Ivica et al., 2014). Briefly, insulated tungsten wires ($\varnothing = 33 \mu\text{m}$) were arranged in a predesigned 3D geometry with typical interwire spacing of $250 \mu\text{m}$ to target both superficial (cortical areas) and deeper structures (such as different nuclei of the thalamus, basal ganglia and midbrain). This type of complex recording geometries are needed for parallel recordings in widely distributed functionally connected networks. The currently investigated arrays were designed to target several parts of the cortico-basal ganglia-thalamic loop to study the selection of behaviors. These complex designs are particularly challenging to build and require a thorough verification of electrode positioning. To test for the general applicability of the methods developed, 3 different electrode designs were evaluated (Rat design #1: rostral and caudal forelimb motor cortex, orbitofrontal cortex, posterior parietal cortex, pre-limbic and infra-limbic cortex, nucleus accumbens, dorsal striatum, hippocampus, the medial geniculate nucleus of the thalamus; Rat design #2: rostral/caudal forelimb and trunk motor cortex, hindlimb sensorimotor cortex and trunk somatosensory cortex, medial/lateral dorsal striatum, globus pallidus pars externa, the sub-thalamic nucleus and substantia nigra pars reticulata; Mouse design:

rostral and caudal motor cortex, medial/lateral dorsal striatum; see Fig. 1),

2.3. Surgical procedures

Details of the surgical procedure are described elsewhere (see e.g. (Bryt et al., 2018)). In short, for electrode implantation, animals were anesthetized with Medetomidinhydrochloride/Fentanyl (0.3/0.3 mg/kg; Apoteket AB, Sweden)) and fixed in a stereotaxic device (David Kopf Instruments, CA, USA) to secure a stable cranium position. The electrode was inserted with a micromanipulator to a specified depth and fixated with dental acrylic cement (Kerr, CA, USA) attaching to screws in the skull. In rats, after surgery, the anesthesia was reversed by Atipamezolhydrochloride (0.5 mg/kg; Apoteket AB, Sweden), and Buprenorphine (0.05 mg/kg; Apoteket AB, Sweden) was administered as postoperative analgesic. In mice, Carprofen (5 mg/kg) was administered once per day for the 5 subsequent days after surgery. Mice and rats were allowed to recover for a minimum of one week after which experiments involving recording of brain activity took place during a couple of months.

2.4. Tissue preparation

After the termination of recording experiments, the rats were anesthetized with a lethal dose of sodium pentobarbital (100 mg/kg i.p., Apoteksbolaget AB, Sweden) and the mice with a high dose of ketamine/xylazine mix (ketamine: 100 mg/kg; xylazine: 12 mg/kg). The heads were then carefully severed and stored in PFA for 1–2 days (due to limited access to the scanner) and then prepared for CT acquisition. When further histological analysis was desired, the animals were instead transcardially perfused with 0.9% saline followed by 4% paraformaldehyde before decapitation. Heads were stored in 4% paraformaldehyde for one week before a CT scan was obtained. After CT acquisition brains from 6 rats were extracted and transferred to 25% sucrose solution in 0.1 M phosphate buffer (PB) at 4°C until sinking for cryoprotection. Coronal sections of $30 \mu\text{m}$ were cut serially through the entire brain using a microtome and stored at -20°C in non-freezing buffer solution. Coronal brain sections were stained with cresyl violet (CV) and compared to CT scans of the implants to verify the placement of each wire.

2.5. Nissl staining

In preparation for the Nissl staining, brain sections were mounted onto chromalum-gelatin coated slides (Thermo Scientific, Menzel-Gläser, Braunschweig, Germany). Sections were stained with 0.5% CV powder in distilled water (dH₂O) and 0.06% acetic acid solution for 15 s. Then, sections were shortly rinsed in dH₂O and dehydrated with 70%, 95% and 99% ethanol and then immersed in xylene for a total of 4 min before coverslipping with dibutylphthalate polystyrene xylene (DPX). The placement of electrodes was evaluated by microscopic analysis.

2.6. CT imaging

For animals scanned in Lund, CT scans were performed on a MILabs XUHR system (MILabs, Netherlands) with the head positioned such that electrode wires were perpendicular to the photon beam in order to minimize metal artifacts (65 kV peak energy, 0.13 mA current, 90 ms exposure time, $200 \mu\text{m}$ Cu filter, $100 \mu\text{m}$ Al filter). Similarly, for animals scanned in Umeå, CT scans were performed on a Mediso Nanoscan PETCT scanner (Mediso, Hungary), also with the electrode wires perpendicular to the photon beam to minimize artifacts, except where noted. The CT was performed as a helical scan with 0.30 pitch, 700 projections with 300 ms exposure time, 70 kV tube voltage, and 72 μA tube current. Images were reconstructed with thin-slice RamLak filter, to give a $30 \mu\text{m}$ side, and $34 \mu\text{m}$ slice thickness. Data were stored in DICOM

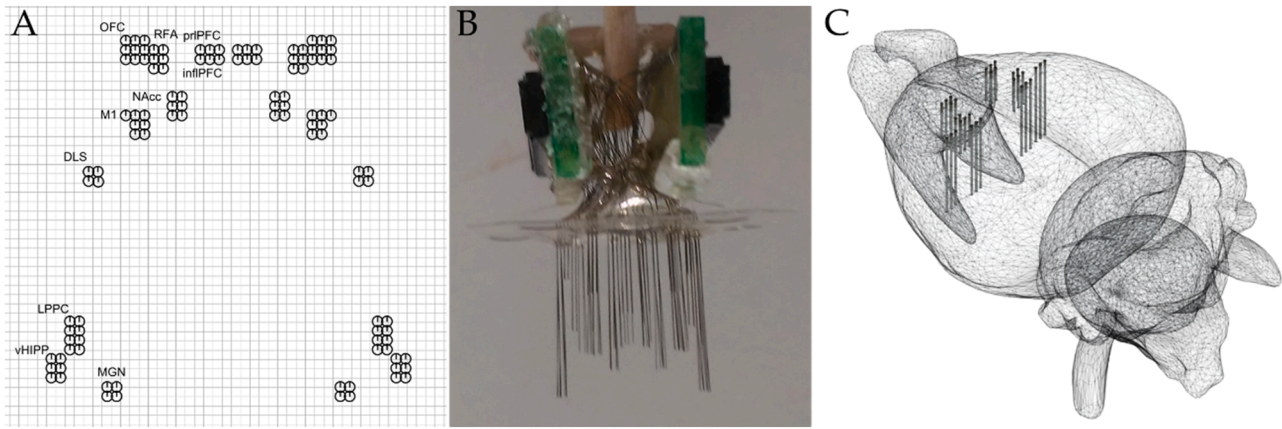


Fig. 1. Illustration of distinct electrode designs for rat and mouse. A) A 2D, top-down view illustration of the mediolateral and anterior-posterior coordinates for each individual recording electrode during the design stage. This is a design for rats targeting 10 distinct structures in each hemisphere (for comparison, in situ, see Fig. 6). B) Photograph of a finished multielectrode array, constructed according to the design shown in the left column, ready for implantation. C) A model of a mouse multielectrode array consisting of 32 wires targeting 4 brain structures per hemisphere, overlaid on an approximate model of the surface of the mouse brain (Free3D, 2021) for illustration purposes.

or NIfTI format and transferred to an off-site server for further processing.

2.7. Comparison between CT and histology

For six of the implanted rats, a comparison between electrode placement evaluated by CT and histology was carried out. Because the precision achievable using histological verification was in most cases not sufficient to determine the placement of each individual electrode tip, we investigated the correspondence between electrode placement determined by CT and histology based on the structure hit by each electrode group instead. For each rat, there was a potential of 10 structures per hemisphere or 20 structures per animal. For some animals, the brain sections were too damaged after brain extraction to define the electrode placement with certainty, and in these animals that specific structure was excluded from further analysis (exact numbers are presented together with the quantitative comparison between histology and CT, Table 5). For each animal, the structure hit by each electrode bundle was evaluated after CT imaging and in Nissl stained sections, where a hit was defined as at least one electrode tip being located within the structure of interest. The percentage match between the two analysis methods was calculated.

2.8. Mock electrode for test of spatial resolution

We constructed a mock electrode array consisting of three coplanar sets of three tungsten wires (approx. 33 μm diameter) glued to a glass slide, each with varying interwire distances of approximately 100 μm , 250 μm and 400 μm . This object was CT scanned as well as observed with microscopy techniques under 10x magnification.

2.9. Software implementation

2.9.1. Programming language

The code developed was implemented in Matlab R2021a, Mathworks Inc. However, in the following subsections, the algorithmic procedures are described in sufficient detail to allow for independent implementation in other programming languages.

2.9.2. Coregistration to image atlas based on anatomical landmarks

When standard anatomical landmarks, including bregma and lambda plus at least one bilateral pair of landmarks, are present and identifiable in the acquired CT volume, it is possible to determine a transformation that puts the CT image in the same space as the Paxinos image atlas of

the Norwegian rat (Paxinos and Watson, 2007) or the Paxinos image atlas of the mouse (Franklin and Paxinos, 2008). In this coregistration procedure, the coordinates of bregma define the translation that makes the origins coincide, and bregma and lambda together define the anterior-posterior direction as well as the scaling factor that adjusts the size of the CT skull to match that of the atlas' brain. The bilateral landmarks in this case are only used to determine the mediolateral direction, so their particular identity is not important.

For convenience, we define the \hat{x} , \hat{y} and \hat{z} axes such that they coincide with the atlas' mediolateral (ML), anterior-posterior (AP) and dorsoventral (DV) directions respectively. The transformation allowing for mapping of the CT image onto the image atlas is calculated as follows: let \vec{B} and \vec{LD} denote the coordinates of bregma and lambda respectively. We calculate the transformation as the composition of distinct components: a translation, scaling, and two rotation components. The translation component is trivially given by:

$$T_{tr} = \begin{bmatrix} 1 & 0 & 0 & -B_x \\ 0 & 1 & 0 & -B_y \\ 0 & 0 & 1 & -B_z \\ 0 & 0 & 0 & 1 \end{bmatrix}$$

The scaling component is calculated in terms of the AP direction vector, calculated as $\vec{AP} = \vec{B} - \vec{LD}$. Then the scaling factor is $S = \frac{\|\vec{AP}\|}{\delta}$, where δ , given in mm, is the fixed bregma-lambda distance in the Paxinos rat atlas, or the equivalent constant for the Paxinos mouse atlas. Then the scaling component is given by:

$$T_{sc} = \begin{bmatrix} S & 0 & 0 & 0 \\ 0 & S & 0 & 0 \\ 0 & 0 & S & 0 \\ 0 & 0 & 0 & 1 \end{bmatrix}$$

The rotation components are determined in two steps. First,¹ a rotation is determined that aligns the image's $\vec{AP} = \frac{\vec{AP}}{\|\vec{AP}\|}$ direction with the \hat{y} axis. This transformation is described in terms of a change of basis operation F^{-1} that rotates the \vec{AP} direction to lie in the xy plane, followed by a rotation G in the xy plane to align \vec{AP} with \hat{y} , followed by the reverse change of basis F to return to the original orientation, with

¹ Following the argument presented in (Ober, K, 2014)

$$F = \left[\widehat{AP} \mid \frac{\widehat{y} - (\widehat{AP} \cdot \widehat{y})\widehat{AP}}{\|\widehat{y} - (\widehat{AP} \cdot \widehat{y})\widehat{AP}\|} \mid \widehat{y} \times \widehat{AP} \right]$$

and

$$G = \begin{bmatrix} \widehat{AP} \cdot \widehat{y} & -\|\widehat{AP} \times \widehat{y}\| & 0 \\ \|\widehat{AP} \times \widehat{y}\| & \widehat{AP} \cdot \widehat{y} & 0 \\ 0 & 0 & 1 \end{bmatrix}$$

with the complete rotation given in block matrix form by:

$$T_{rotAP} = \begin{bmatrix} FGF^{-1} & 0 \\ 0 & 1 \end{bmatrix}$$

Next, another rotation is determined that aligns the image's ML direction with the \widehat{x} axis. Unlike the AP direction, which is univocally determined by bregma and lambda, the image's ML direction may be ill-defined depending on the particular set of landmarks determined by the user. In the general case, let $\{\vec{L}_{pre}\}$ be the set of landmarks that lie to the left of the midline, $\{\vec{R}_{pre}\}$ be the set of landmarks that lie to the right of the midline, and $\{\vec{M}_{pre}\}$ be the set of landmarks that are exactly on the midline. Assuming that the translation component and the previously defined rotation component have already been determined, then let

$$\{\vec{L}\} = \{T_{tr}T_{rotAP}\vec{L}_{pre}\}$$

$$\{\vec{R}\} = \{T_{tr}T_{rotAP}\vec{R}_{pre}\}$$

$$\{\vec{M}\} = \{T_{tr}T_{rotAP}\vec{M}_{pre}\}$$

be the corresponding sets of transformed landmarks. Then,

$$a = \argmin_a \{ \|M_x \cos(\alpha) + M_z \sin(\alpha)\| + \|(L_x - R_x) \sin(\alpha) - (L_z - R_z) \cos(\alpha)\| \}$$

is the angle that simultaneously minimizes the difference between the DV components of the left and corresponding right landmarks, and the distance between the midline landmarks and the yz plane. Once a has been determined, the final rotation is given by:

$$T_{rotML} = \begin{bmatrix} \cos(a) & 0 & \sin(a) & 0 \\ 0 & 1 & 0 & 0 \\ -\sin(a) & 0 & \cos(a) & 0 \\ 0 & 0 & 0 & 1 \end{bmatrix}$$

Finally, the complete transformation is given by $T = T_{sc}T_{rotML}T_{rotAP}T_{tr}$.

2.9.3. Manual adjustment of coregistration

To allow the user to inspect the results of applying the calculated transformation, the software enables the possibility to create and display snapshots of the superimposition of each atlas slice and the corresponding plane of the transformed CT image. If the calculated transformation leads to an unsatisfactory match between atlas and CT, the software allows the user to incrementally adjust individual components of the transformation, such as translation magnitudes and rotation angles, until the user is satisfied by the visual inspection of the superimposition. The adjusted transformation T' is constructed by means of perturbing the original transformation T as follows:

$$T' = T'_{sc}T'_{rotML}T'_{rotAP}T'_{tr}.$$

where the individual components for non-uniform scaling, rotations and translation are constructed according to user-supplied parameters.

2.9.4. Coregistration to volumetric atlas

As long as a subset of at least three non-colinear landmarks among 12 pre-determined ones are visible in the CT image, it is also possible to

perform coregistration between the image and the Waxholm volumetric atlas (Papp et al., 2014). This is especially useful when bregma and/or lambda are not present in the CT image, for example because of an extensive craniotomy, when the smaller number of cranial landmarks defined in the Paxinos atlases can make coregistration less viable. The transformation that puts the CT image in the same space as the Waxholm atlas is calculated as follows²: let

$$P_0 = \begin{bmatrix} x_{1,i} & y_{1,i} & z_{1,i} \\ \vdots & \vdots & \vdots \\ x_{N,i} & y_{N,i} & z_{N,i} \end{bmatrix}^T$$

be the $3 \times N$ set of coordinates corresponding to the landmarks determined by the user, and

$$Q_0 = \begin{bmatrix} x_{1,f} & y_{1,f} & z_{1,f} \\ \vdots & \vdots & \vdots \\ x_{N,f} & y_{N,f} & z_{N,f} \end{bmatrix}^T$$

the corresponding set of known coordinates for the same landmarks in the Waxholm atlas. Let also.

$P = P_0 - [\bar{x}_i \ \bar{y}_i \ \bar{z}_i]^T \mathbf{1}_N^T$ and $Q = Q_0 - [\bar{x}_f \ \bar{y}_f \ \bar{z}_f]^T \mathbf{1}_N^T$ be the corresponding sets after translation such that the respective centroids coincide with the origin.

Then $M = QP^T(P P^T)^{-1}$ is the ordinary least squares solution that minimizes the error associated with the transformation $Q = MP$, and, provided the set of landmarks is free from outliers and spans the volume of the skull to a reasonable extent, then M is the least-squares optimal transformation matrix that transforms the CT space into the atlas space.

M defines a 9-parameter, non-rigid transformation whose decomposition may include a reflection component. In order to remove reflections, allowing only rotation and (possibly non-uniform) scaling, it is convenient to calculate the singular value decomposition of the matrix M in the form $M = U \Sigma V^T$. Then, the presence of reflections can be checked by inspecting the sign of the determinant of VU^T , and in the general case can be accounted for by letting (Umeyama, 1991)

$$M = U \Sigma \begin{bmatrix} 1 & 0 & 0 \\ 0 & 1 & 0 \\ 0 & 0 & \text{sgndet} VU^T \end{bmatrix} V^T$$

Finally, the translation component can be recovered by $t = -M[\bar{x}_i \ \bar{y}_i \ \bar{z}_i]^T + [\bar{x}_f \ \bar{y}_f \ \bar{z}_f]^T$, and the full transformation becomes:

$$T = \begin{bmatrix} M & t \\ 0 & 1 \end{bmatrix}$$

2.9.5. Coordinate transformations between Waxholm space and stereotaxic space

To facilitate comparisons between the Waxholm atlas (SD v1.01) and the stereotaxic atlas (Paxinos and Watson, 2007) we have defined transformations that can be used to go between the two coordinate systems. Unfortunately, there is no single best solution to this problem and different compromises will have to be made depending on the use case. Hence, we included three transformations in this package: *Papp*, *Modified Papp* and *Anisotropic*:

2.9.5.1. Papp. This transformation follows (Papp et al., 2016) and performs a pitch rotation of -4.085° around bregma and a uniform scaling of 1.057. However, this transformation puts the (Waxholm space) WHS lambda 0.37 mm above the horizontal bregma plane in the Paxinos space, and it also puts the WHS lambda and the WHS origin 0.08 mm off the medial plane.

² Following the argument presented in (Kluev, E, 2013)

2.9.5.2. Modified Papp. If a better alignment of the bregma and lambda reference points is preferred, it can be achieved with a slight modification of the Papp transform: a scaling of 1.0491, a pitch of -6.489° , a yaw of -0.5395° and a roll of 0.5675° . The scaling factor was calculated as the proportion between the bregma-lambda distances in the two atlases. A major issue with this transformation is the inaccurate scaling in the ML and DV directions.

2.9.5.3. Anisotropic. The scaling mismatch can only be improved with anisotropic scaling. By using the most lateral edges of the deep cerebral white matter (DCW) as reference points, we calculated an ML scaling factor of 0.9412. The DV scaling factor was defined as the proportion between the bregma-WHS origin distances in the two atlases (0.9244). For AP scaling and rotations we used the same values as in the modified Papp transform.

In summary, the anisotropic transformation gives the smallest overall error and should be the preferred choice in most situations, given that anisotropic scaling is not a problem (Table 1). Note however that any of these transformations only solve for coordinate system transformations as defined in the two atlases, which does not imply a good match between brain structures (Table 2). For example, we noted that the distance between the skull and the superficial edge of the cortex varies significantly between the two atlases.

2.9.6. Electrode segmentation algorithm – initialization

The segmentation algorithm operates plane by plane along the dorsoventral direction, which is assumed to be roughly parallel to the direction of the individual electrodes, and takes as input a pre-selected ROI spanning 6 continuous planes (the “reference planes”) as well as the known fixed number of electrode cross-sections present in those planes.

With the number of electrodes known, the algorithm first searches the defined area of the first (i.e. the most dorsal) reference plane for a corresponding number of high intensity (HI) pixels, subject to the constraint that any two candidate HI pixels cannot be closer to each other than a selectable minimum distance. During the search, HI pixels are defined as pixels with an intensity equal to or higher than a determined percentage of the maximum intensity observed within the search area. This threshold percentage is iterated starting from a very high level (90%), which typically leads to very few candidate HI pixels being accepted, and decreased stepwise until a number of candidate HI pixels equal to the known number of electrodes is found, and the algorithm returns successfully. Alternatively, a number of candidate HI pixels exceeding the known number of electrodes may be found, or the threshold may be decreased below a set limit (60%), when in both cases the algorithm reports a failure state instead.

If the search is completed successfully, the algorithm attempts to improve on the candidate HI pixels by running successive rounds of optimization where each candidate HI pixel is moved towards the local intensity maximum in a small 1-pixel neighborhood around it, while still subject to the minimum distance constraint between all pairs of candidate HI pixels, until no further improvement is possible. The algorithm then moves on to the next reference plane, using the positions of the

candidate HI pixels determined during the previous step as the initial guess for the search.

Once the six reference planes have been searched and the expected number of candidate HI pixels has been determined for each plane, it is necessary to attribute labels to the candidate HI pixels such that each label, and thus each corresponding electrode, maintains a coherent identity along the reference planes. The algorithm accomplishes this by attributing labels arbitrarily for the first plane, and then, for each subsequent plane, assigning labels to each candidate HI pixel while subject to the constraint that the distance between pixels with the same label in consecutive planes cannot be larger than a fixed fraction (40%) of the minimum distance between candidate HI pixels in the same plane, i.e., a fixed fraction of the constraint applied in the previous step. The matching that obeys this constraint, when it exists, is found by constructing the pairwise distance matrix between candidate HI pixels in the current plane and the previous plane, applying the desired distance cutoff to the distance matrix to obtain the logical matrix of acceptable matchings, and passing the result to the *matchpairs* MATLAB routine to solve the corresponding linear assignment problem. This step is important to avoid mislabeling of pixels when the general direction of the electrodes in the array deviates substantially from the direction perpendicular to the CT planes in the (presumed) horizontal slices, (i.e. the dorsoventral direction), a situation that is prone to causing labels to “jump” between neighboring electrodes (Fig. 2).

2.9.7. Electrode segmentation algorithm

The algorithm segments each wire individually, plane by plane, towards the ventral direction and starting from the last reference plane. For a given wire, at each step, the algorithm fits a 3D line through the previously segmented pixels belonging to the same wire over the previous P planes, and uses it to project the expected geometric continuation of the wire onto the next plane.

Following (Söderkvist, 2009), the line of best fit through the last P planes is calculated by horizontally stacking the coordinates of the corresponding P pixels in a $3 \times P$ matrix C_0 ,

$$C_0 = \begin{bmatrix} x_1 & y_1 & z_1 \\ \vdots & \vdots & \vdots \\ x_P & y_P & z_P \end{bmatrix}^T$$

subtracting the centroid of that matrix from each column,

$$C = C_0 - [\bar{x}_i \quad \bar{y}_i \quad \bar{z}_i]^T \mathbf{1}_P^T$$

then applying the singular value decomposition $C = U\Sigma V^T$ and taking the first corresponding left-singular vector $[U_{11} \ U_{21} \ U_{31}]^T$. Then, the pixel that corresponds to the geometric continuation of the line of best fit in the subsequent plane is given by

$C' = [\bar{x} \ \bar{y} \ \bar{z}]^T + \frac{(z_P - 1) - \bar{z}}{U_{31}} [U_{11} \ U_{21} \ U_{31}]^T$. Once the putative geometric continuation of the wire is determined, the algorithm creates a small 1-pixel neighborhood around that center and finds the pixel corresponding to the local intensity maximum inside that neighborhood. The intensity of this pixel is compared to the average intensity of

Table 1
Coordinates in Paxinos after transformation from WHS.

Transformation	Bregma (B)	Lambda (λ)	WHS origin (O)	DCW left	DCW right	Distance B-L	Distance B-O	Distance left-right DCW
Papp	0.0000	-0.0826	-0.0826	-7.2702	7.1050	8.7686	8.0241	14.3752
	0.0000	-8.7604	-0.6708 – 7.9956	-6.7896	-6.7896			
	0.0000	0.3678		-6.8960	-6.8960			
Modified Papp	0.0000	-0.0000	-0.0000	-7.0842	7.1827	8.7033	7.9644	14.2682
	0.0000	-8.7033	-0.3331	-6.5137	-6.3793			
	0.0000	0.0000	-7.9574	-7.1919	-7.0506			
Anisotropic	0.0000	-0.0000	-0.0000	-6.3552	6.4436	8.7033	7.0196	12.8001
	0.0000	-8.7033	-0.3331	-6.5137	-6.3793			
	0.0000	0.0000	-7.0117	-6.3371	-6.2126			

Table 2
Coordinates of reference points in the Waxholm atlas and the Paxinos atlas. Dimensions are in the order ML, AP, DV. Coordinates are positive in the right, anterior and superior directions. Units are in mm.

Atlas	Bregma (B)	Lambda (L)	WHS origin (O)	DCW left	DCW right	Distance B-L	Distance B-O	Distance left-right DCW
Waxholm	0.0781250 ^a	0 ^a	0 ^a	-6.8	6.8	8.29570157	7.59140267	13.60000000
	1.1718750 ^a	-7.0703125 ^a	0 ^a	-5.7 1.45	-5.7 1.45			
	7.5000000 ^a	8.43750000 ^a	0 ^a					
Paxinos & Watson	0 ^b	0 ^b	0 ^b	-6.4	6.4	8.70329670	7.00446286	12.80000000
	0 ^b	-8.70329670 ^b	-0.5	-6.48	-6.48			
	0 ^b	0 ^b	-7	-5.5	-5.5			

Other coordinate values were estimated by the authors.
^a Values defined in https://www.nitrc.org/docman/view.php/1081/2095/Coordinates_v1-v1.01.pdf
^b Values defined in (Paxinos and Watson, 2007). The AP coordinate of lambda in the Paxinos atlas was calculated as $(9.1-0.3) \cdot 9/9.1$

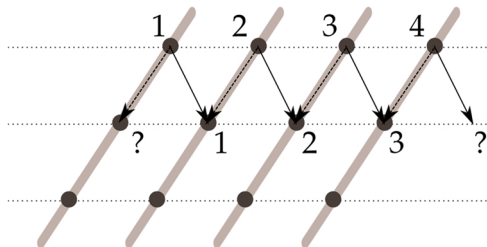


Fig. 2. Example illustration of ambiguous mapping between adjacent image planes. The presence of parallel wires with small interwire distances relative to the scan resolution, the broadening of wire thicknesses due to metal-induced artifacts, and the predominant wire directions being slightly diagonal with respect to the direction perpendicular to the horizontal CT planes can in this situation create conditions for naively-assigned labels to “jump” between neighboring wires. Conditions are exaggerated for illustrative purposes.

segmented pixels in the previous P planes, and this pixel is recorded if this relative intensity is at least 80% of the running average, or discarded otherwise. This process is then repeated iteratively for P ranging from 60 to 6 planes, though it cannot be larger than the number of previously segmented planes, and all distinct possible continuations are recorded. If more than one possible continuation is identified for a given plane, the algorithm selects the one that corresponds to the largest P, thus

privileging smooth curves of large radius and a corresponding relative stiffness of electrodes. If no possible continuations are identified, the last segmented plane is deemed to contain the recording tip of the current wire and appropriately noted, and the algorithm moves on to the next electrode.

3. Results

3.1. Choice of scanning angles influence spatial resolution due to variable shadowing effects

It is a well-known problem in clinical CT imaging that metal implants tend to cause artefacts that shade and limit the image quality in the nearby tissue volume (for example, dental amalgams are a common source of artefacts in head and neck CT images (Branco et al., 2020)). To assess the magnitude of this problem in our context, we scanned electrode arrays with two distinct electrode array designs (Fig. 1), in situ, in the heads of euthanized rats and mice. We observed that the relationship between the dominant direction of the electrodes in the array (dorsal-ventral direction in our case) and the plane that contains the X-ray beams plays a major role in the origin of metal artefacts (Fig. 3). Based on these results, we conclude that the best reconstruction is obtained when the CT is acquired with the dominant direction of the electrodes being perpendicular to the plane that contains the beams, which can be achieved by placing the head on its side inside the tunnel such that the

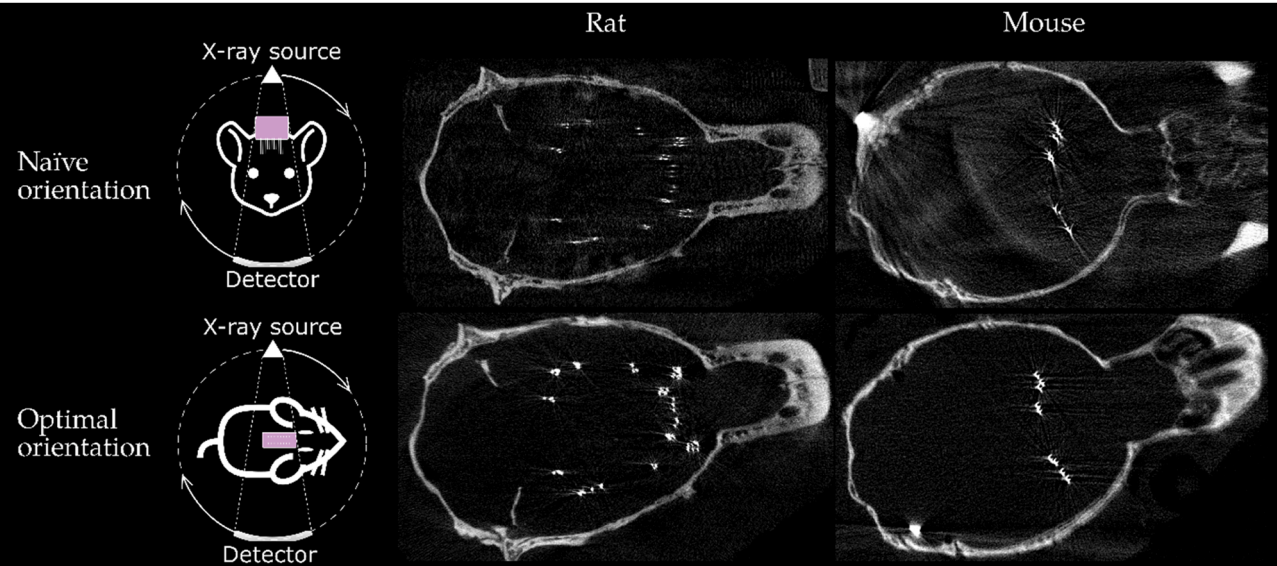


Fig. 3. Comparison between CT images for a rat and a mouse, acquired with the head positioned in naïve orientation (prone position) in the tunnel (top) vs. rotated to be lying on its side, with the snout pointing sideways, in such a way that the dominant direction of the electrodes is parallel to the tunnel direction and perpendicular to the X-ray beams (bottom). Metal artefacts are reduced and signal quality is improved when the image is acquired in the latter orientation. Illustrations adapted from the following Wikimedia Commons files under public domain or CC-BY-SA licenses: [\[https://commons.wikimedia.org/wiki/File:\]](https://commons.wikimedia.org/wiki/File:Mouse_cartoon.svg)Mouse-cartoon.svg, OpenMoji-black_1F42D.svg, PrincipCT.svg..

tunnel axis is aligned with the DV direction.

3.2. Resolution of CT images – comparison to ground truth obtained with optical techniques

To obtain an estimate of the spatial resolution practically attainable through CT imaging, we constructed and scanned a mock electrode and compared the CT images with a set of microscopy images of the same object (Fig. 4). Under the conditions investigated, it was feasible to discern individual wires in the CT image at an interwire distance of 250 μm and larger, but not at a 100 μm interwire distance.

Furthermore, it was clear that the reconstructed wires appeared thicker in the CT image, probably due to the combined effects of 1) the CT sampling and the reconstruction algorithm as well as 2) as a consequence of artifacts induced by the material, resulting in a small amount of uncertainty in the actual position of the tips. At a CT resolution of 34.3 μm , and for a wire thickness of about 30 μm , the wire thickness is overestimated by a factor of about 3x, corresponding to an uncertainty in the tip position of ± 1 pixel or ± 34.3 μm at the current resolution used in our CT reconstructions.

However, this limitation in image reconstruction will in most instances not constitute a major limitation as long as center coordinates for the respective tips can be estimated with acceptable precision. Therefore, we subsequently tested the uncertainty in CT-based estimates of relative electrode positions by measuring the distances between wire tips as observed in the CT image, compared to the same distances measured under an optical microscope (Table 3). For the distance measurements, the RMS deviation between the microscope and CT measurements corresponded to 15 μm at this resolution. It can be noted that this uncertainty is of the same order as the size of the typical cells being recorded from, thus approaching the spatial limits of what could be considered a meaningful spatial resolution in the context of extra-cellular single unit recordings.

3.3. Analysis workflow

Following these initial evaluations indicating an adequate spatial resolution for the intended purposes, given appropriate scanning

position of multi-electrode arrays, we designed a software package consisting of a set of Graphical User Interfaces (GUIs) implementing the developed algorithms. In our software solution, the data analysis workflow consists of three steps: 1) Pre-processing of newly acquired scans, 2) Coregistration of the images to an anatomical atlas, and 3) Segmentation of the individual electrodes in the image to allow automatic procedures to determine the exact location of the electrode tips (Fig. 5). Although broadly similar, the analysis workflow depends on whether the user initially elects to align the image to a volumetric or image atlas (the respective advantages and trade-offs related to this choice are further addressed in the Discussion section). After completing these three processing steps, the software outputs the calculated stereotaxic coordinates for the tip of each electrode with respect to a cranial reference point (e.g. bregma), and optionally superimposes the CT and atlas images to allow the user to visually determine the anatomical structure that contains the tip of each electrode. In a typical user case, the entire analysis requires about 2–3 h. In the standard procedure, as described herein, the Paxinos rat/mouse atlases are used, but adaptation to other brain spaces is also addressed in the Discussion section.

3.3.1. GUI 1: CT pre-processing

As described in Section 3.2, the heads should optimally be scanned in a position where the X-ray beams are perpendicular to the electrodes in order to minimize the artefacts induced by the metal electrodes (Fig. 3). For this reason, the standard positioning assumed in CT scanning software rarely matches the actual head positioning. Hence, the reconstructed image will typically have mislabeled axes, e.g., the 2D projection labeled “Coronal” may show a sagittal view etc. To permit coordinate realignment to software labels, the *preprocess_ct* GUI allows the user to load an acquired CT image in DICOM or Nifti format and permute the coordinates in the raw data while maintaining a positively oriented coordinate system, so that the axes are then correctly labeled. Moreover, in this step the user is also able to crop the image in all three axes in order to reduce file size and discard extraneous information.

3.3.2. GUI 2: coregistration to an anatomical atlas

Once the image has been cropped and rotated to a standard orientation, the *register_landmarks* GUI allows the user to perform a

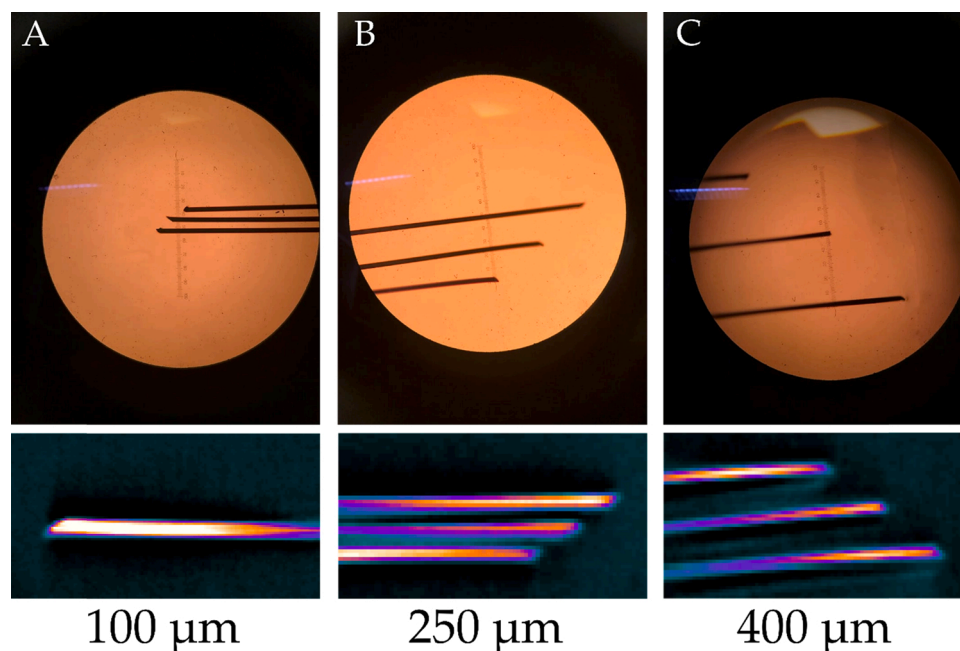


Fig. 4. Comparison between microscopy and CT imaging of a mock microelectrode array consisting of 3 coplanar sets of 3 wires with approximately 100, 250, and 400 μm spacing both parallel and perpendicular to the wire lengths, observed under the microscope at 10x magnification. Tick spacing is 10 μm . Electrodes spaced 100 μm were not distinguishable from each other in the CT scan taken at a resolution of 34.3 μm , despite the thickness of the wires being approximately 30 μm .

Table 3

Parallel (horizontal) and perpendicular (vertical) distances, given in micrometers, between electrode tips in CT, measured as distance in pixels from (presumed) center to center multiplied by scan resolution (34.3 μm), rounded to the nearest integer and given in μm .

	100 μm				250 μm				400 μm			
	Parallel		Perpendicular		Parallel		Perpendicular		Parallel		Perpendicular	
Electrode pair	Mic	CT	Mic	CT	Mic	CT	Mic	CT	Mic	CT	Mic	CT
Short-Mid	130	–	70	–	360	343	220	206	570	583	460	480
Mid-Long	80	–	80	–	320	309	240	240	500	515	500	480

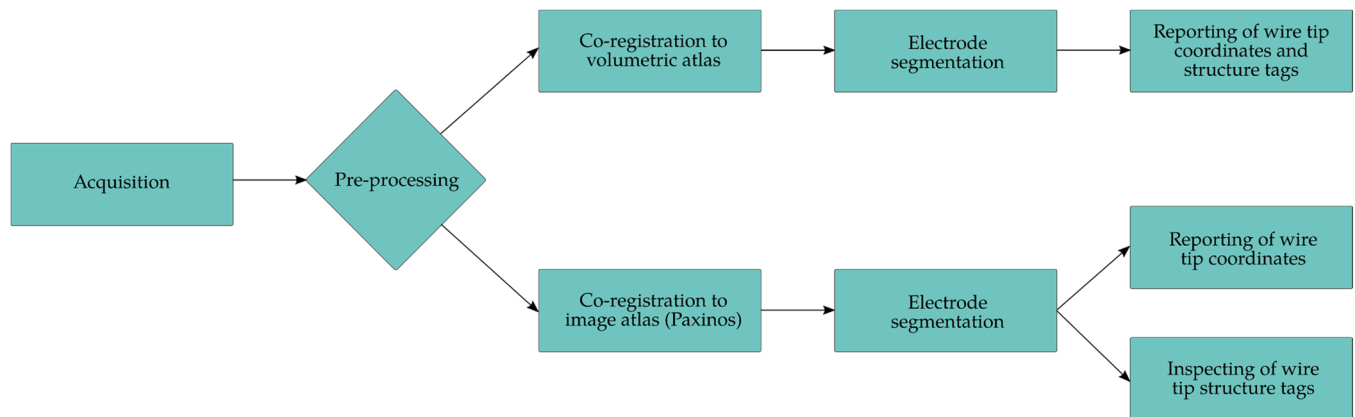


Fig. 5. Illustration of typical analysis workflow. Each step is mostly automatized but may require some user input. The decision to perform coregistration to a volumetric atlas or to an image atlas depends mostly on data-independent concerns and is made early on during the analysis process.

coregistration between the CT image and a selected volumetric or image atlas. This step requires the user to inspect the image for a small number of anatomical landmarks, typically bregma, lambda, plus one bilateral pair, that are used to calculate the mathematical transformation that puts the CT image in the same space as the atlas. The *register_landmarks* GUI accepts a list of 12 pre-defined anatomical landmarks that are easily identifiable in CT images of the skull. The full list of currently pre-defined landmarks can be found in (Table 4).

Table 4

List of landmarks acceptable for coregistration with the volumetric Waxholm atlas. The precise coordinates and images can be obtained together with the software packages.

Name	Short description
Bregma	Standard anatomical landmark.
Lambda	“
Cranial fossa, left	The superiormost orbit of the top of the petrosal bone, sitting superior to the parafoveoli.
Cranial fossa, right	“
Maxillary canal, left	The ventralmost visible opening of the maxillary canal in the most medial curve of the left maxillary bone. Note: alternatively, this could be ethmoidal canals
Maxillary canal, right	“
Occipital condyle, left	In the horizontal view of the caudalmost interparietal bone, the posteriormost margin of occipital condyles.
Occipital condyle, right	“
Interparietal bone	In the axial view of the caudalmost interparietal bone, the medial point of the line of best fit along the dorsalmost caudalmost margin.
Foramen magnum	In the sagittal plane, the superior most margin of the foramen magnum in the occipital bone.
Basisphenoid bone	The ventralmost and caudalmost point along the midline of the basisphenoid bone.
Frontal bone	The dorsomedialmost point of the frontal bone, forming the ceiling of the olfactory cavity.
WHS origin	Decussation of the anterior commissure; <i>not a skull landmark</i> .

3.3.3. GUI 3: electrode segmentation

Once the CT image has been coregistered to atlas and the corresponding mathematical transformation has been calculated, the *identify_electrodes* GUI allows the user to segment all the individual electrodes in the electrode array and determine the voxel corresponding to each electrode tip with a semi-automatized procedure. The default parameter settings assume that the individual electrodes are mostly parallel to each other and traverse the brain in the dorsoventral direction.

This analysis stage is divided into a number of successive processing steps, and requires user input at a few critical points. In the first step, the user is required to locate a horizontal plane in which all electrodes are clearly visible and separated in such a way that, using the known electrode layout, the individual electrode identities can later be easily matched to the numbers attributed to the corresponding recording channels in the electrophysiological acquisition system. A plane with these characteristics is likely to be located very dorsally, in many cases outside the skull. In the selected plane, the user is required to indicate the center of each electrode with a marker, either individually, electrode by electrode, or, if the user has access to an electrode map containing the intended anatomical coordinates for each electrode, this mapping can be loaded from a file for all electrodes at once, and applied to the CT image using the inverse of the transformation calculated with the *register_landmarks* GUI to transform anatomical coordinates into CT voxels.

With the centers of the electrodes indicated in the reference plane (Fig. 6), the software segments the electrodes in two stages. First, a set of cylinder-shaped ROIs with a fixed radius of a few pixels are created, one centered on each marker and extending down six planes in the ventral direction, while keeping each electrode inside its respective cylinder for all planes. Based on these ROIs, the corresponding number of electrodes (i.e. the number of markers inside these cylinders) are modeled in an “initialization” step intended to determine the characteristic direction and pixel intensity of each electrode. Low signal-to-noise or merged electrodes may require this step to be repeated with slight changes to the parameters until the GUI reports that a satisfactory initial segmentation has been achieved.

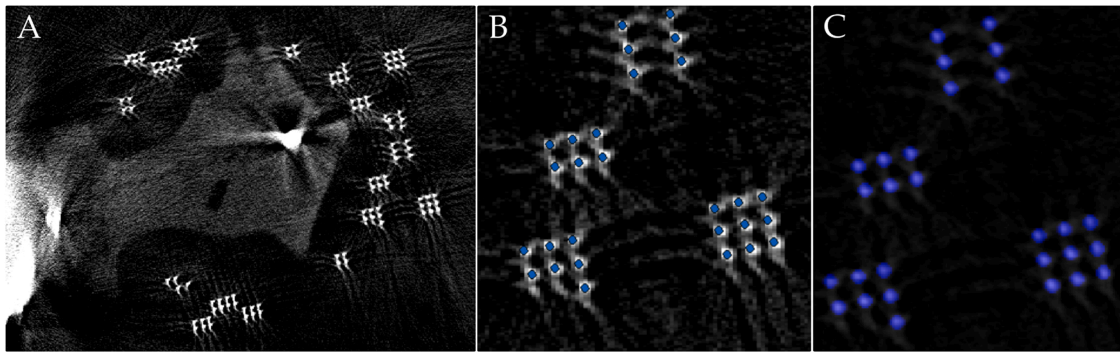


Fig. 6. First stage of electrode segmentation. A) Horizontal slice of CT scan at the level of bregma, with compressed dynamic range to help illustrate the tailored shape of the craniotomies as well as the design of the multielectrode array. Note the position of bregma and lambda marked by drops of silver paint applied during surgery. B) For automatized identification of the channel identity of individual wires in the larger array, the multielectrode array design is loaded from a file and applied to the image using the affine transformation calculated in the previous step. Small automatic and manual adjustments are sometimes required to ensure that each marker (turquoise) corresponds to the center of one individual wire. C) ROIs (dark blue) are automatically created around each marker and subsequently used to determine each wire's characteristic direction and intensity in the “initialization” step of the segmentation.

Once the reference planes have been successfully segmented and the expected number of electrodes has been identified and coherently labeled, the GUI creates a plot with all the electrode identities and positions that can be used to match the arbitrarily-attributed electrode labels with the channel numbers attributed by the electrophysiology acquisition software. The algorithm also uses the segmentation obtained during the initialization to ascertain the characteristic intensity and direction of the center of each electrode, information that is used in the subsequent segmentation steps.

Following successful completion of this initialization step, the software automatically segments all electrodes down to their respective tips according to the methods described above, placing a new marker at the corresponding location. Notably, however, a few potential complications can arise at this stage. When a microelectrode array is constructed out of thin, long and relatively flexible individual electrodes, it can happen that two neighboring electrodes get pushed together during the implantation process and their recording tips end up in locations very close to one another, or possibly merged with respect to the image resolution. On other occasions, a single electrode can bend when being inserted, often due to not being perfectly perpendicular to the brain surface at the point of insertion and thus being subjected to lateral forces that push the trajectory progressively further from the intended direction. If the bent electrode touches or passes close to another electrode, this can lead to a point crossing in the CT traces, i.e. it appears in certain image planes as if the two electrodes are merged. These and other unexpected situations where the electrode tips for some reason are not segmented appropriately by the automated procedures can be manually corrected in a subsequent processing step. The *identify_electrodes* GUI allows the user to perform this step by simply dragging the marker that corresponds to the tip of the electrode to the correct position, as well as to correct its dorsoventral coordinate if necessary. In a typical use case, manual corrections were found to be necessary for less than 10% of the wires in a 128ch-electrode array.

When all electrodes have been successfully segmented and the voxels corresponding to the electrode tips have been determined, the transformation calculated in the previous step using the *register_landmarks* GUI can be used to obtain the anatomical coordinates of the electrode tips. If only stereotaxic positions are required, the coordinates and corresponding electrode labels are then simply exported to an output file. For applications where it is desirable to annotate coordinates of the electrode tip locations with anatomical data from a standard brain space, the final processing step (also handled by the *identify_electrodes* GUI) uses the calculated transformation to superimpose the corresponding CT plane on each atlas slice and export merged images where electrode tips are marked and anatomical delineations are visible. This

set of images can be used to manually verify the structure hit by each electrode, a process that takes a few seconds per electrode.

3.4. Comparison between CT and histology in example slices

As mentioned in the introduction, full 3D reconstruction of the distribution of electrode tip coordinates based on microscopic analyses of fixated and stained brain section is next to impossible to perform for the type of electrode designs evaluated here (i.e. over 100 electrodes distributed in a large number of brain structures). Thus, a comprehensive quantitative comparison between coordinates estimated from CT and histology would not be meaningful. Nevertheless, because histological verification is still widely used for these purposes, it may be informative to perform a direct comparison in at least a few example slices where histological analyses appear to give reliable indications. Indeed, when comparing the results of the semi-automatic CT-based segmentation of multi-electrode arrays with the determination of electrode tip placement in one example brain via histological analysis, a high degree of correspondence was observed. Essentially, most electrode tips were assigned to the same structure using both methods and although a certain difference in terms of the exact tip locations was observed, these differences were relatively minor (Fig. 7). Unfortunately, the precision using histological verification was not sufficient to identify each individual wire in correspondence with the design of the multielectrode array, and sometimes not even sufficient to determine the placement of each individual electrode tip (when using 30 μm wires arranged in groups, with 250 μm spacing between wires; see also Fig. 1). Thus, what was sometimes seen in the Nissl stained brain slices was in most cases the trace left by each group of electrodes. To mitigate this problem, we decided to instead compare electrode placement correspondence between CT and histology in six implanted rats based on the structure hit by each electrode group, where a hit was defined as at least one electrode tip being located within the structure of interest. This comparison revealed a 90% correspondence between the results from the two methods (Table 5).

4. Discussion

We have here described the workflow and the precise algorithms needed for efficient verification of electrode tip placement in the small brain of rodents, also for complex multi-electrode geometries targeting a large number of structures in parallel. To our knowledge, previously described methods, although incorporating certain related processing steps, do not enable the user to create an estimate of the detailed electrode locations with comparable precision and with the same relatively

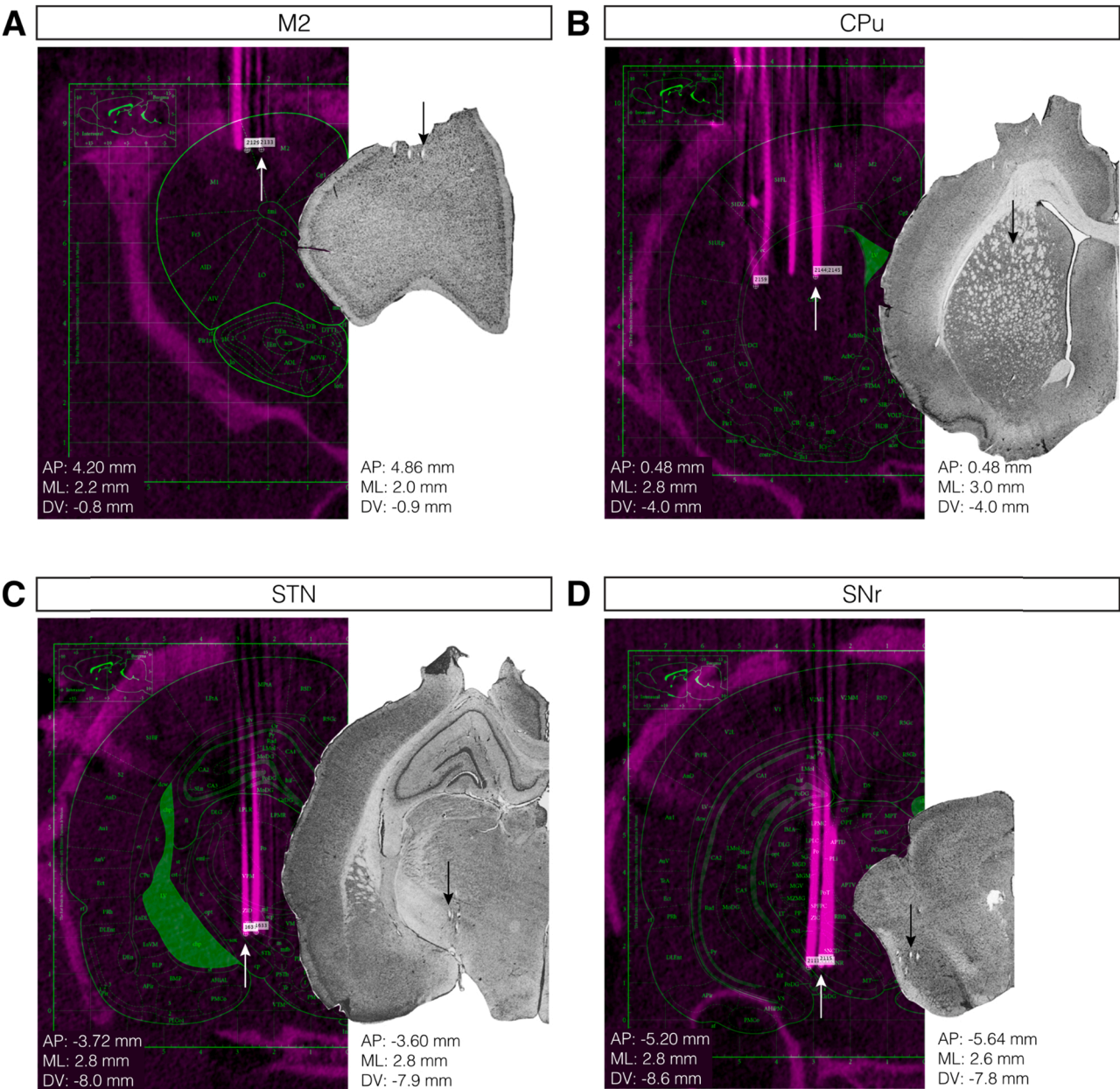


Fig. 7. Comparison between results of histological analysis and CT segmentation for selected coronal planes of one example brain. A-D. CT segmentation (left) and Nissl stained coronal brain sections (right) of one example brain for (A) secondary motor cortex (M2), (B) striatum (CPu), (C) subthalamic nucleus (STN), and (D) substantia nigra pars reticulata. Arrows indicate electrode tips which placement is presented in coordinates based on the Paxinos rat atlas. The selected slices show a relatively good agreement between histological analysis and CT segmentation regarding the structure hit by each wire, as well as relatively small absolute deviation between the calculated wire tip coordinates (see also Table 5).

Table 5
Comparison between results of histological analysis (Nissl) and CT segmentation in rats.

Animal	Structure match between CT and Nissl	Structure mismatch between CT and Nissl	Excluded structures	Percentage structure match between CT and Nissl
#1	12	1	7	92%
#2	10	4	6	71%
#3	16	1	3	94%
#4	14	2	4	88%
#5	16	2	2	89%
#6	18	0	2	100%
Total	86	10	24	90%

limited work effort. For example, Borg and co-authors described a method based on coregistration of acquired CT images of implanted animals to an existing Magnetic Resonance Imaging (MRI) atlas (Borg et al., 2015). However, the method was designed to assign bundles of electrodes to structures at least 1 mm in each dimension rather than individual electrodes and did not provide means to automatically locate the recording tips. In an alternative approach, Masís et al. described a method based on CT imaging of osmicated brains (Masís et al., 2018), which however required the recording electrodes to be cut in situ or removed from the tissue, making this procedure less suitable for the purposes discussed here. Additionally, Paglia et al. recently described a software toolkit that facilitates the superimposition of images of histological slices onto an atlas of the rat brain for reconstruction of probe tracks and subsequent 3D visualization (Paglia et al., 2021), but this

method also requires the user to manually trace the track of implanted probes. Finally, in a recent publication, Király et al. describe a method for in vivo localization of electrodes that is based on the acquisition and simultaneous co-registration of 3 distinct sets of images: a pre-implantation CT scan, a pre-implantation MRI, and a post-implantation CT scan (Király et al., 2020). While their analysis pipeline shares important similarities with the method described here, they do not report automated methods for neither image to atlas co-registration nor segmentation of electrodes from a CT image, and indeed the workflow appears to be dominantly manual, which does not scale adequately for the simultaneous segmentation of over a hundred individual recording electrodes as reported here. Furthermore, we here make the tools reported available as a software package, which may be of value to the community. Hence, in comparison to these methods, the procedures described herein have a number of important advantages. In particular, the developed methods make it possible to automatically follow the trajectory of individual closely spaced neighboring electrodes, to algorithmically determine the voxel coordinates that correspond to the recording tip of each electrode and, by means of coregistration to an anatomical atlas of choice, to report the standardized coordinates of the recording target in addition to broader structure tags. Furthermore, this can be achieved without the need for sophisticated data acquisition pipelines, pre-processing of the animal samples (such as fixation and/or further chemical tissue processing) or post-imaging histological analyses. It can be noted, that the developed techniques could, in principle, be applied also to the brain of a larger animal. However, this would require an increased field of view without compromising spatial resolution.

However, a few limitations of the described methods deserves to be mentioned. We found that metal electrodes should preferably be oriented perpendicular to X-ray beams upon acquisition of the CT scans. While this geometrical constraint was not a limiting factor using heads from euthanized rodents, it may be a limiting factor for the image quality of scans obtained in live animals with electrode implants in a similar geometry since a perpendicular positioning in relation to the X-ray beams will not be achievable in most CT machines. Although fully automatized procedures may not generate accurate estimates in this situation, manual segmentation will in most cases allow for accurate marking of electrode tips (as described in Section 3.3.3), at the cost of substantially increased analysis time.

Furthermore, although outside the scope of our current method development, a number of well-known general limitations in brain imaging studies applies also to the developed technology. In particular, two main limitations ought to be mentioned. First, each individual brain has to be mapped onto a standard brain model via non-isotropic transformations to allow for anatomical annotation of structures (Collins et al., 1995). These transformations are typically made by adjustment of the brain hull to the interior surface of the cranium, which inevitably will display variations between strains, sexes and individuals. Second, a standard reference brain for rodents does not exist and the most widely used rodent atlases do not fully match each other. The developed method offers the user the possibility to perform coregistration to either the Paxinos or the Waxholm atlases, and each alternative has distinct advantages and disadvantages; the Paxinos atlas of 2D tissue sections for rat and mouse is widely used in the research community, but requires slightly more manual interventions to optimize the transformation between spaces and anatomical annotation of structures, whereas the volumetric pre-segmented Waxholm atlas of the rat brain supports greater automation in coregistration and is more flexible with respect to cranial landmarks but can often be too imprecise in segmentation and annotation and may therefore require manual, ad hoc segmentation. It can be noted, that the recent introduction of contrast-enhanced CT imaging of the brain could in the future potentially greatly facilitate co-registration with an atlas by providing more information on soft tissue structures but at present often requires highly specialized techniques (Kastner et al., 2020; Camilieri-Asch et al., 2020; Llambrich et al.,

2020; Chen et al., 2018). Finally, of note, the Paxinos atlas is based on a male Wistar rat, while the Waxholm atlas is based on a male Sprague-Dawley rat; users performing cross-strain/-sex coregistration, as in the current study, may therefore need to consider differences in brain dimensions, particularly for more posterior coordinates.

The neuroscientific research community, is seeing a rapidly growing number of in vivo studies using chronic implants consisting of large number of electrodes (Steinmetz et al., 2018; Schwarz et al., 2014; Tamtè et al., 2016) or optical fibers, miniscope optics, etc. (Aharoni et al., 2019; Sych et al., 2019). Thus, the demand for reliable, less time-consuming procedures for anatomical reconstruction of implantation coordinates is steadily increasing. In this view, the methods developed herein could potentially find wider use. Crucially, when entering a new age of data sharing, information about the exact sensor location will be essential to allow for pooling or comparisons between different studies (Bjerke et al., 2018). We therefore foresee a further development of the methods presented herein in line with the technologies used in the human brain-imaging field. In this context, we believe the procedures presented in this paper can serve as an important first stepping-stone in this exciting future scientific and engineering endeavor.

Funding

The study was supported by grants from the Kempe Foundation, Insamlingsstiftelserna, Oskarfonden, Umeå University, The Swedish Brain Foundation, Vinnova, Vetenskapsrådet (VR) Grant 2018–02717 and Grant 2021–01769, The Child Cancer Foundation, The Parkinson Foundation, Kockska Foundation, Hedlund Foundation, Åhlén Foundation, Promobilia, LU Innovation. The computations were enabled by resources provided by the Swedish National Infrastructure for Computing (SNIC) at LUNARC partially funded by the Swedish Research Council through grant agreement no. 2016–07213, Wenner-Gren foundation.

CRediT authorship contribution statement

Luciano Censoni: Conceptualization, Methodology, Software, Data curation, Formal analysis, Visualization, Writing – original draft, Writing – review & editing. **Pär Halje:** Conceptualization, Methodology, Software, Data curation, Formal analysis, Writing – review & editing. **Jan Axelsson:** Conceptualization, Writing – review & editing. **Katrine Skovgård:** Validation, Investigation, Formal analysis, Visualization, Writing – review & editing. **Arash Ramezani:** Investigation, Visualization, Writing – review & editing. **Evgenya Malinina:** Writing – review & editing. **Per Petersson:** Conceptualization, Supervision, Project administration, Funding acquisition, Writing – original draft, Writing – review & editing.

Competing interest

The authors declare no competing interest.

Data availability

The manuscript contains a link to the software developed in this study.

Acknowledgments

The authors wish to thank Madelene Ericsson for skilled assistance in performing the CT scans, Ann-Christin Lindh for excellent technical assistance in performing the Nissl staining, and Sebastian Sulis Sato, Sebastián Barrientos and Abdolaziz Ronaghi for skilled assistance with surgical implantation as well as revision of preliminary versions of the manuscript and Fahad Sultan for expert advice with respect to

anatomical nomenclature as well as revision of preliminary versions of the manuscript. For algorithmic procedures, the authors wish to acknowledge the following insightful StackExchange answers and associated discussion (Kluev, 2013; Ober, 2014).

References

- Aharoni, D., Khakh, B.S., Silva, A.J., Golshani, P., 2019. All the light that we can see: a new era in miniaturized microscopy. *Nat. Methods* 16, 11–13. <https://doi.org/10.1038/s41592-018-0266-x>.
- Bjerke, I.E., Øvsthus, M., Papp, E.A., Yates, S.C., Silvestri, L., Fiorilli, J., Pennartz, C.M.A., Pavone, F.S., Puchades, M.A., Leergaard, T.B., Bjaalie, J.G., 2018. Data integration through brain atlas: Human Brain Project tools and strategies. *Eur. Psychiatry* 50, 70–76. <https://doi.org/10.1016/j.eurpsy.2018.02.004>.
- Borg, J.S., Vu, M., Badea, C., Badea, C., Johnson, G.A., Dziras, K., 2015. Localization of metal electrodes in the intact rat brain using registration of 3D microcomputed tomography images to a magnetic resonance histology Atlas. *eNeuro* 2 (4), 1–14. <https://doi.org/10.1523/ENEURO.0017-15.2015>.
- Branco, D., Kry, S., Taylor, P., Rong, J., Zhang, X., Peterson, C., Frank, S., Followill, D., 2020. Development of a stereoscopic CT metal artifact management algorithm using gantry angle tilts for head and neck patients. *J. Appl. Clin. Med. Phys.* 21, 120–130. <https://doi.org/10.1002/ACM2.12922>.
- Brys, I., Halje, P., Scheffer-Teixeira, R., Varney, M., Newman-Tancredi, A., Petersson, P., 2018. Neurophysiological effects in cortico-basal ganglia-thalamic circuits of antidyskinetic treatment with 5-HT 1A receptor biased agonists. *Exp. Neurol.* 302, 155–168. <https://doi.org/10.1016/j.expneurol.2018.01.010>.
- Camilieri-Asch, V., Shaw, J.A., Mehnert, A., Yopak, K.E., Partridge, J.C., Collin, S.P., 2020. diceCT: A Valuable Technique to Study the Nervous System of Fish. *eNeuro* 7, 1–23.
- Campbell, P.K., Jones, K.E., Huber, R.J., Horch, K.W., Normann, R.A., 1991. A Silicon-Based, Three-Dimensional Neural Interface: Manufacturing Processes for an Intracortical Electrode Array. *IEEE Trans. Biomed. Eng.* 38, 758–768. <https://doi.org/10.1109/10.83588>.
- Chen, K.C., Arad, A., Song, Z.M., Croaker, D., 2018. High-definition neural visualization of rodent brain using micro-CT scanning and non-local-means processing. *BMC Med. Imaging* 18.
- Collins, D.L., Evans, A.C., Holmes, C., Peters, T.M., 1995. Automatic 3D segmentation of neuro-anatomical structures from MRI. In: Bizais, Y., Barillot, C., Di Paola, R. (Eds.), *Proc. Information Processing in Medical Imaging*. Kluwer Academic Publishers, Dordrecht, The Netherlands.
- Dziras, K., Fuentes, R., Kumar, S., Potes, J.M., Nicolelis, M.A.L., 2011. Chronic in vivo multi-circuit neurophysiological recordings in mice. *J. Neurosci. Methods* 195, 36–46. <https://doi.org/10.1016/j.jneumeth.2010.11.014>.
- Franklin, K.B.J., Paxinos, G., 2008. *The Mouse Brain in Stereotaxic Coordinates*, 3rd ed., Academic Press/Elsevier, Amsterdam; Boston.
- Free3D, 2021. Mouse Brain 3D. (<https://free3d.com/3d-model/mouse-brain-3d-1906.html>).
- Hanson, T.L., Diaz-Botia, C.A., Kharazia, V., Maharbiz, M.M., Sabes, P.N., 2019. The “sewing machine” for minimally invasive neural recording. *bioRxiv*, 578542. <https://doi.org/10.1101/578542>.
- Ivica, N., Tamtè, M., Ahmed, M., Richter, U., Petersson, P., 2014. Design of a high-density multi-channel electrode for multi-structure parallel recordings in rodents, in: 36th Annual International IEEE EMBS Conference of the IEEE Engineering in Medicine and Biology Society. pp. 393–396. (<https://doi.org/10.1109/EMBC.2014.6943611>).
- Kastner, D.B., Kharazia, V., Nevers, R., Smyth, C., Astudillo-Maya, D.A., Williams, G.M., Yang, Z., Holobetz, C.M., Santana, L., Della, Parkinson, D.Y., Frank, L.M., 2020. Scalable method for micro-CT analysis enables large scale quantitative characterization of brain lesions and implants. *Sci. Rep.* 10.
- Király, B., Balázsfi, D., Horváth, Solari, N., Sviatkó, K., Lengyel, K., Birtalan, E., Babos, M., Bagaméry, G., Máthé, D., Szigeti, K., Hangya, B., 2020. In vivo localization of chronically implanted electrodes and optic fibers in mice. *Nat. Commun.* Sep 17 (1), 4686. <https://doi.org/10.1038/s41467-020-18472-y>.
- Kluev, E., 2013. Finding translation and scale on two sets of points to get least square error in their distance?, (<https://stackoverflow.com/a/14525705>). Accessed in 2022-02-21.
- Llambrich, S., Wouters, J., Himmelreich, U., Dierssen, M., Sharpe, J., Gsell, W., Martínez-Abadías, N., Vande Velde, G., 2020. ViceCT and whiceCT for simultaneous high-resolution visualization of craniofacial, brain and ventricular anatomy from micro-computed tomography. *Sci. Rep.* 10.
- Masís, J., Mankus, D., Wolff, S.B.E., Guitchounts, G., Joesch, M., Cox, D.D., 2018. A micro-CT-based method for quantitative brain lesion characterization and electrode localization. *Sci. Rep.* 8 <https://doi.org/10.1038/s41598-018-23247-z>.
- Ober, K., 2014. Calculate Rotation Matrix to align Vector A to Vector B in 3d?, (<https://math.stackexchange.com/a/897677>). Accessed in 2022-02-21.
- Paglia, J., Saldanha, P., Fuglstad, J.G., Whitlock, J.R., 2021. TRACER: a toolkit to register and visualize anatomical coordinates in the rat brain, (<https://www.biorxiv.org/content/10.1101/2021.10.01.462770v1>).
- Papp, E., Leergaard, T., Calabrese, E., Johnson, G., Bjaalie, J., 2014. Waxholm Space atlas of the Sprague Dawley rat brain. *Neuroimage* 97, 374–386. <https://doi.org/10.1016/j.neuroimage.2014.04.001>.
- Papp, E., Leergaard, T., Csucs, G., Bjaalie, J., 2016. Brain-wide mapping of axonal connections: workflow for automated detection and spatial analysis of labeling in microscopic sections. *Front. Neuroinform.* 10, Article 11.
- Paxinos, G., Watson, C., 2007. *The Rat Brain in Stereotaxic Coordinates*, 6th ed., Academic Press/Elsevier, Amsterdam; Boston.
- Schwarz, D.A., Lebedev, M.A., Hanson, T.L., Dimitrov, D.F., Lehw, G., Meloy, J., Rajangam, S., Subramanian, V., Ifft, P.J., Li, Z., Ramakrishnan, A., Tate, A., Zhuang, K., Nicolelis, M.A.L., 2014. Chronic, wireless recordings of large scale brain activity in freely moving rhesus monkeys. *Nat. Methods* 11, 670. <https://doi.org/10.1038/NMETH.2936>.
- Söderkvist, I., 2009. Using SVD for some fitting problems. (<https://www.ltu.se/cms/fs/1.51590/svd-fitting.pdf>).
- Steinmetz, N.A., Koch, C., Harris, K.D., Carandini, M., 2018. Challenges and opportunities for large-scale electrophysiology with Neuropixels probes. *Curr. Opin. Neurobiol.* <https://doi.org/10.1016/j.conb.2018.01.009>.
- Stensola, H., Stensola, T., Solstad, T., Frøland, K., Moser, M., Moser, E.I., 2012. The entorhinal grid map is discretized. *Nature* 492, 72–78. <https://doi.org/10.1038/nature11649>.
- Sych, Y., Chernysheva, M., Sumanovski, L.T., Helmchen, F., 2019. High-density multi-fiber photometry for studying large-scale brain circuit dynamics. *Nat. Methods* 16, 553–560. <https://doi.org/10.1038/s41592-019-0400-4>.
- Tamtè, M., Brys, I., Richter, U., Ivica, N., Halje, P., Petersson, P., 2016. Systems-level neurophysiological state characteristics for drug evaluation in an animal model of levodopa-induced dyskinesia. *J. Neurophysiol.* 115, 1713–1729. <https://doi.org/10.1152/jn.00868.2015>.
- Umeyama, S., 1991. Least-squares estimation of transformation parameters between two point patterns. *IEEE Trans. Pattern Anal. Mach. Intell.* 13 (4), 376–380. <https://doi.org/10.1109/34.88573>.